APPLICATION OF ANALYSIS ON GRAPHS TO SITE-BOND MODELS FOR DAMAGE EVOLUTION IN HETEROGENEOUS MATERIALS

ANDREY P. JIVKOV[*†], TODOR S. TODOROV[†], CRAIG N. MORRISON[†] AND MINGZHONG ZHANG[†]

[*] Research Centre for Radwaste and Decommissioning, School of Earth, Atmospheric and Environmental Sciences, The University of Manchester
Oxford Road, Manchester M13 9PL, UK
e-mail: andrey.jivkov@manchester.ac.uk, www.rcrd.manchester.ac.uk

[†] Modelling and Simulation Centre, School of Mechanical, Aerospace and Civil Engineering, The University of Manchester
Oxford Road, Manchester M13 9PL, UK

Key Words: Microstructure; Lattice-spring model; Discrete calculus; Micro-cracking

Summary. This work demonstrates the use of discrete exterior calculus for efficient solution of lattice models for quasi-brittle media. Applications to the mechanical behaviour of cement pastes and nuclear graphite are shown. Real microstructures are represented by a topologically averaged regular complex of 3D cells. Microstructure details, such size distribution and density of particles and pores, are mapped to the complex to determine geometrical and mechanical properties of cell elements. The complex is reduced to a lattice, the site-bond model, represented as a mathematical graph embedded in 3D. The technology for solving the model with discrete calculus is presented. Porosity effects on the materials elastic properties are analysed to demonstrate agreement with experimental data. Further, the evolution of macroscopic damage is analysed as emerging from the generation and growth of micro-crack population. The results agree very well with measured stress-strain behaviour of the materials. This suggests that the theory can be used for deriving damage evolution as well as cohesive laws for continuum based modelling of fracture in quasi-brittle media.

1 INTRODUCTION

Damage in heterogeneous materials is a mechanism for dissipation of strain energy, often associated with the generation and growth of micro-cracks. Initially these are of the size of specific microstructure features, but consequently coalesce to form larger micro-cracks. Specifically, quasi-brittle materials, such as cements, graphite and rocks, have elastic-brittle behaviour at the microstructure length-scale, resulting in micro-cracking, but show non-linear behaviour at engineering length-scales often referred to as "gracefulness". The link between evolving micro-crack populations and the emergent longer-scale behaviour can provide insights into the microstructure-failure relations.

Application of continuum-based strategies to analyse microstructure-controlled evolution

of micro-crack populations is unrealistic. A realistic methodology needs to account for the heterogeneity and the mechanisms of micro-crack generation. Discrete lattice models provide frameworks for incorporating relevant materials information. Lattices are based on cellular architectures, where sites located in cells are linked by bonds resisting relative deformations. Relation between bond properties and continuum can be established either by matching bond forces to cell stresses [1, 2], or by equating strain energies in the bonds and the cell [3, 4]. The latter can be used for deriving explicit bond-continuum relations for regular lattices. In 2D, lattices based on hexagonal cells are the most widely used, as they can represent isotropic materials with Poisson's ratio up to 1/4 in plane strain and up to 1/3 in plane stress with springs of positive stiffness [4, 5]. In 3D, it was shown that lattices based on SC, HCP and FCC arrangements could represent only isotropic materials with zero Poisson's ratio [5]. Thence, realistic simulations of micro-cracking have been performed on 2D hexagonal structures [6, 7]. Real crack morphologies, however, are non-planar and an appropriate lattice is required for simulating crack spatial evolution.

The site-bond method [8], based on a tessellation of space into truncated octahedral cells, was shown to reproduce a wide range of isotropic material. With bonds represented by beams, the methodology was used to predict damage evolution in cement under tension and compression [9] and concrete under complex loadings [10]. The method was further developed to represent bonds by spring bundles [11]. A new formulation, allowing for the incorporation of a richer set of microstructure characteristics, was proposed and applied to nuclear graphite [12]. This work presents a development in the generation of microstructure-informed site-bond models for materials which can be idealised as three-phase media: stiff inclusions in a compliant matrix containing pores. Further, an application of analysis on graphs [13] for the solution of 3D deformation-damage problems is given. Finally, the proposed methodology is used for the analysis of cement paste and nuclear graphite. The focus is on the effect of aging in cement and of irradiation in graphite on the mechanical behaviour. These are communicated to macroscopic level through pore system changes.

2 PHYSICAL AND MECHANICAL MODELLING

2.1 Topological averaging

The media we consider contain two sized features, stiff particles and pores, distributed randomly in a compliant matrix. It is assumed that the size distribution and the volume density of the two types of features are known from experiment, e.g. computer X-ray tomography. In principle, one can use directly a 3D image of a real microstructure and create an irregular cell complex, e.g. by constructing the Voronoi diagram of the particle set. In such case the pore set will be distributed within the cells. An irregular lattice can then be constructed by connecting the centres of neighboring cells in the Voronoi tessellation. This image-based modeling approach is useful for calibrating lattice element properties with in-situ tomography (4D imaging), but difficult to justify for up-scaling. Moreover, without experimental data the calibration of the lattice element properties is not feasible. Therefore, regularity in the cell complex representing the microstructure is preferable.

We perform this regularization, or geometric homogenization, using a complex of compactly packed truncated octahedral cells, Fig. 1a, considering that a cell of this shape represents the average neighbourhood of a particle in a material [8]. This complex represents

the physical space with geometric characteristics fully determined by one length parameter. Selected here is the distance, S, between two parallel square faces. With this, the cell volume is $V = S^3/2$, the area of the eight hexagonal faces is $A_1 = S^2 3\sqrt{3}/16$, and the area of the six square faces is $A_2 = S^2/8$. The cell complex is reduced to a mathematical graph by placing sites (graph nodes) at the centres of all cells and bonds (graph edges) between neighbouring sites as illustrated in Fig. 1b. The bonds are eight normal to hexagonal faces (nearer neighbours) denoted by B_1 with length $L_1 = S\sqrt{3}/2$ and six normal to square faces (further neighbours) denoted by B_2 with length $L_2 = S$.
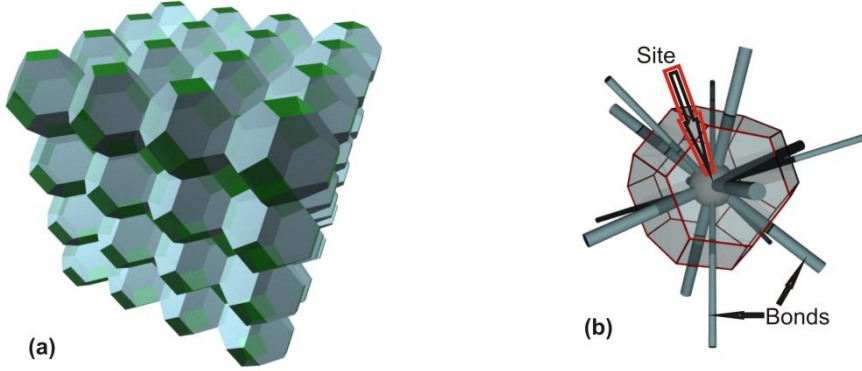
Figure 1: Cell complex as basis for lattice construction: (a) fragment illustrating compact tessellation of a three-phase medium into cells, with each cell representing the average neighbourhood of particles; and (b) cell neighbourhood illustrating graph elements to which experimental information is mapped.

2.2 Feature-free lattice mechanics

The bond resistance to relative displacements between adjacent sites is represented by one axial (normal to cell face) and two transverse (tangent to cell face) springs, forming a proper orthogonal system. The two transverse springs in a bond have identical stiffness. Hence, site interactions are characterised by four constants, K_1, T_1, K_2 and T_2, the stiffness coefficients of axial and transverse springs in bonds B_1 and B_2, respectively. The constants are determined for locally linear displacement field by equating the energy in a continuum cell and half the energy in the 14 bonds [11]. The relations between the elasticity tensor and the constants are:

$$C_{iiii} = \frac{2}{3S}\left(K_1 + 2T_1 + 3K_2\right), \quad for\ i = 1, 2, 3 \tag{1}$$

$$C_{iijj} = \frac{2}{3S}\left(K_1 - T_1\right), \quad for\ i \neq j\ and\ i, j = 1, 2, 3$$

$$C_{ijij} = \frac{2}{3S}\left(K_1 + 2T_1 + 3T_2\right), \quad for\ i \neq j\ and\ i, j = 1, 2, 3$$

Notably, the lattice represents cubic elasticity, but the system is over-determined and allows for infinitely many choices for the inverse relations. In our applications $T_2 = 0$ is selected. This leads to the results for cubic elasticity, using Voigt notations C_{11}, C_{12} and C_{44}, and for isotropic elasticity, using Young's modulus E and Poisson's ratio ν, given by Eq. (2). With positive K_1, K_2 and T_2, the lattice could represent isotropic materials with Poisson's ratio

in the range $-0.5 \leq v \leq 0.25$; a substantial improvement from previous 3D lattices which allowed for $v = 0$ only [5]. Extension for materials outside this interval is possible with negative spring stiffness. It should be realized that bond energies represent area energies on faces. Area energies are not necessarily positive definite quadratic forms of strains [13, 14]. The spring constants correspond to coefficients of the surface stiffness tensor and hence need not be positive as long as the total bond energy is positive. The results reported here are for isotropic materials with $-0.5 \leq v \leq 0.25$, so spring stiffness is positive.

$$K_1 = \frac{S}{2}(C_{44} + 2C_{12}); \quad T_1 = \frac{S}{2}(C_{44} - C_{12}); \quad K_2 = \frac{S}{2}(C_{11} - C_{44}) \tag{2}$$

$$K_1 = \frac{ES(1+2v)}{4(1+v)(1-2v)}; \quad T_1 = \frac{ES(1-4v)}{4(1+v)(1-2v)}; \quad K_2 = \frac{ES}{4(1+v)(1-2v)}$$

2.3 Microstructure to model mapping

Since a cell is topologically averaged particle neighbourhood, particles are placed in all cells of the complex with remaining volume occupied by matrix and pores. This, together with experimental data for size distribution, $F(c)$, and volume density, θ_c, of particles is used for calculating the model characteristic length. By distributing spherical particles with radii c_i from $F(c)$ to a number of cells, N_c, the cell size is calculated as:

$$S = \sqrt[3]{\frac{8\pi}{4} \sum_{N_c} c_i^3 \Big/ N_c \theta_c} \tag{3}$$

Spherical pores of radii d_i from experimental size distribution $F(d)$, are mapped randomly to cell faces until their cumulative volume reaches $V\theta_d$, where $V = N_c S^3/2$ is the total volume of the complex, and θ_d is the experimental pore volume density. The allocation is such that the great circle of a pore is on a face to create the worst case scenario for initial face area reduction. Notably, the mapping of volume-less (crack-like) defects could proceed in a similar way, but number instead of volume density would be required. The pore mapping affects a set of faces, so that their initial areas, A_i, are reduced to effective areas $a_i = A_i - \pi d_i^2$.

2.4 Feature-modified lattice mechanics

In the absence of pores, the spring constants can be calculated with Eq. (3) for known macroscopic elastic constants. These will represent a system averaged matrix-particle response. In the presence of pores, the measured macroscopic constants, E and v, will be affected. The pore-free spring constants, K_α, T_α ($\alpha = 1,2$), need to be calibrated further so that the dependence of macroscopic properties on porosity observed experimentally can be simulated. The pore effect is represented by local changes of spring constants. As a first approximation the ratio between bond spring constants and bond associated area is fixed. The extent to which this approximation is valid is a subject of ongoing investigation. Presently, the pore-modified spring constants, k_α, t_α, are given by

$$\frac{k_\alpha}{K_\alpha}\left(\frac{t_\alpha}{T_\alpha}\right) = \frac{a_\alpha}{A_\alpha} = 1 - \frac{\pi d^2}{A_\alpha}, \quad \alpha = 1,2 \tag{4}$$

In principle, the calibration of the pore-free K_α, T_α can be made with macroscopic E and ν, measured at two different porosities. This can be achieved by the steps: use arbitrary selection of E and ν to calculate K_α, T_α by Eq. (2); populate two models with the two pore systems; modify the spring constants by Eq. (4); calculate macroscopic properties of the models; determine the actual K_α, T_α by comparison to the two experimental sets of E and ν. This work uses a simplified calibration by assuming that ν is unaffected by porosity change. The pore-free spring constants are determined by one set of macroscopic properties at a given porosity.

In addition to K_α, T_α, the pores affect bond failure, which is related to the matrix separation energy, γ, a material parameter. The bond failure energy is $G_i = \gamma \, a_i$, with $0 \leq G_i \leq \gamma \, A_i$ depending on the allocated pore. Overall bond behaviour is shown schematically in Fig. 2. Force F and displacement u can be positive or negative, but axial springs are not allowed to fail in compression. The initial spring constant, k_α, defines the response to damage initiation point (F_c, u_c). Linear damage evolution is assumed to full separation at (0, $m \, u_c$). It is noted that this is similar to cohesive zone models and potentially overly simplifies bond behaviour. More rigorous definition using lower scale simulations is a subject of ongoing work.
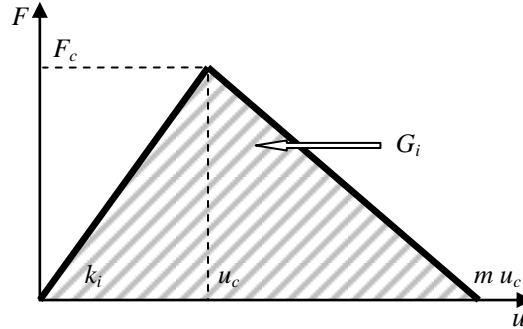
Figure 2: Schematic spring mechanical behaviour

2.5 Macroscopic elastic and damage behaviour

A model bounded by planes $X_1 = 0$, $X_1 = 20S$, $X_2 = 0$, $X_2 = 20S$, $X_3 = 0$, $X_3 = 20S$ was used for numerical simulations, where the coordinate system (X_1, X_2, X_3) was normal to square cell faces. Boundary conditions normal to each plane were only applied, i.e. for plane X_i, normal displacements and forces of nodes were U_i and F_i while other displacements and rotations were unconstrained. For a plane where reaction forces were determined from analysis, the macroscopic stress normal to the plane was calculated as the ratio between the total reaction force and the boundary area, i.e. $\sigma_i = \Sigma F_i / 400S^2$. For a plane where nodal displacements were determined from analysis, the macroscopic strain normal to the plane was calculated as the ratio between the average displacement and the model length, i.e. $\varepsilon_i = \Sigma U_i / (21^2 \times 20S)$.

The calculation of macroscopic Young's modulus and Poisson's ratio was performed from uniaxial tensile or compression simulation in a standard way using the above stress and strain. Micro-cracking was simulated by failure of bonds according to Fig. 2. The macroscopic damage was measured by the relative change of the Young's modulus, $D = 1 - E / E_0$, where E_0 was the initial value for which the lattice local properties were calibrated. The simulations were performed to maximum load; post-peak behaviour was not simulated.

3 MATHEMATICAL FORMULATION AND COMPUTATION

The discrete view of the material is conveniently described by the terminology of algebraic topology. The base entity in the theory is a p-cell, σ_p, defined as a set of points homeomorphic to a closed unit p-ball $B_p = \{x \in \mathrm{R}^p : |x| \le 1\}$. A collection of p-cells defines a p-complex if: (1) the boundary of each p-cell (for $p > 0$) is a union of lower-order p-cells; and (2) the intersection of any two cells is either empty or a boundary element of both cells. With this terminology, the complex in Fig. 1(a) is a 3-complex. Each cell is a 3-cell with faces 2-cells, edges 1-cells and vertices 0-cells. The site-bond model, produced by reduction of this 3-complex, is a 1-complex embedded in R^3 with bonds being 1-cells and sites being 0-cells.

Discrete exterior calculus provides the apparatus for analysis of such discrete spaces [13]. Each p-cell is oriented by specifying a node order and may have one of two possible orientations. Main role in the theory plays the cell boundary, $\partial\sigma_p$, which is homeomorphic to the unit ball boundary $\partial B_p = \{x \in \mathrm{R}^p : |x|=1\}$. The complex boundary is represented by the incidence matrix N_p, with coefficients $n^p_{ij} = 0$ if $\sigma_{p-1,j}$ is not on the boundary of $\sigma_{p,i}$; $n^p_{ij} = +1$ if $\sigma_{p-1,j}$ is on the boundary of $\sigma_{p,i}$ and coherent with its induced orientation; $n^p_{ij} = -1$ if $\sigma_{p-1,j}$ is on the boundary of $\sigma_{p,i}$ and not coherent with its induced orientation.

A p-chain, τ_p, is an n_p-tuple which assigns an object to each p-cell, where n_p is the number of distinct p-cells in the complex. In the classical theory the objects are scalars [13], but we introduce an extension to R^3 vectors to represent displacements and forces. Applying N_p^T to a p-chain results in a $(p-1)$-chain of objects, i.e. $\tau_{p-1} = \mathrm{N}_p^\mathrm{T}\,\tau_p$. Hence, N_p^T is the matrix representation of the discrete boundary operator, $\mathrm{N}_p^\mathrm{T} : C_p \to C_{p-1}$, where C_p denotes the vector space of p-chains. Thus, N_p^T provides both a representation of the topology of the discrete manifold *and* of the boundary operator ∂_p. This is very useful for simultaneous analysis of structure and property of discrete systems. For a basis of chains $\lambda_i \in C_p$ one can use scalar product to define a metric tensor $g^p_{ij} = <\lambda_i, \lambda_j>$. For orthogonal basis, i.e. $g^p_{ij} = 0$ for $i \ne j$, the metric tensor is represented by an $n_p \times n_p$ diagonal matrix of objects $\mathrm{G}_p = \mathrm{diag}(g^p_{ii})$.

A p-cochain is a linear functional that maps a p-chain to objects at each p-cell. The vector space of p-cochains is C^p. Pairing between chains and cochains is equivalent to integration in continuum analysis and uses a coboundary operator, d_p, defined by the discrete analogue of the fundamental theorem of calculus $[d_p c^{p-1}, \tau_p] = [c^{p-1}, \mathrm{N}_p^\mathrm{T}\,\tau_p]$, where c^p is a p-cochain and τ_p is a p-chain. The coboundary operator is given by $d_p = \mathrm{N}_p : C^{p-1} \to C^p$. Converting a p-chain into its equivalent p-cochain is given by $c^p = \mathrm{G}_p\,\tau_p$. The inverse mapping from p-cochains to p-chains can be computed using the inverse of the metric tensor G_p^{-1}.

These preliminaries allow for formulating discrete boundary value problems for the site-bond model as a 1-complex. For compactness, the incidence matrix N_1 and inverse metric tensor G_1^{-1} are denoted by A and K, respectively. For n sites and m bonds, dim(A)$= n \times m$ and dim(K) $= n \times n$. 0-cochain, u, assigns displacement vectors (R^3 objects) to each 0-cell (site). The coboundary operator d_1 is the gradient of these displacements, a 1-cochain. Physically, this means that Au assigns relative displacement vectors to each 1-cell (bond). The 1-cochain is converted to a 1-chain of force vectors, f, using the metric K, so that $f = \mathrm{K}\,\mathrm{A}\,u$. Note, that each diagonal element of K is a 3×3 diagonal matrix with coefficients equal to local axial and transversal spring stiffness. Finally, the boundary operator τ_0 represents the divergence of these forces, which is a 0-chain. This divergence must equal zero for equilibrium at sites and allows for the formulation of the boundary value problem on the graph as follows:

6

$$A^T K A u = b,$$
(5)

where b is a 0-chain of force vectors. Note that $L = A^T K A$ is the discrete Laplace operator and it is symmetric. Prescribed forces at sites enter directly b. Prescribed displacements are imposed in a standard manner as in finite element method. The symmetry of L suggests two approaches for solving the linear system (5): direct solver based on Cholesky decomposition of L; and iterative solver based on the conjugate gradient method. Both approaches have been implemented in an in-house code, taking advantage of efficient algorithms for sparse matrix-vector manipulations. The iterative solver was found to be much faster than the direct solver.

The described formulation is a natural approach for dealing with discrete topologies and can be extended to 3-complexes, which is a subject of ongoing work. The key point is that approximations, such as shape functions in finite elements, are avoided. The only approximation is imposed by the selection of the discrete topology. Further, generation of micro-cracks with zero metric (stiffness) coefficients does not create problems for the solution, as far as the 1-complex remains connected. The in-house code implementing the formulation was used to solve the problems in the next section.

4 RESULTS AND DISCUSSION

4.1 Cement paste

The cement paste studies were on ASTM type I Portland cement with water-to-cement (w/c) ratio 0.5. The microstructure information was acquired with high-resolution computed tomography (micro-CT) at a spatial resolution of 0.5 µm and a source voltage of 59 kV after 7 and 28 days of aging. Images and details of processing can be found in [16]. Obtained microstructure characteristics are: porosities at curing ages of 7 and 28 days are 18.72% and 12.58%, respectively; particle volume fractions are 15.67% and 8.65%, respectively. The size distributions of pores and anhydrous cement particles are shown in Fig. 3.
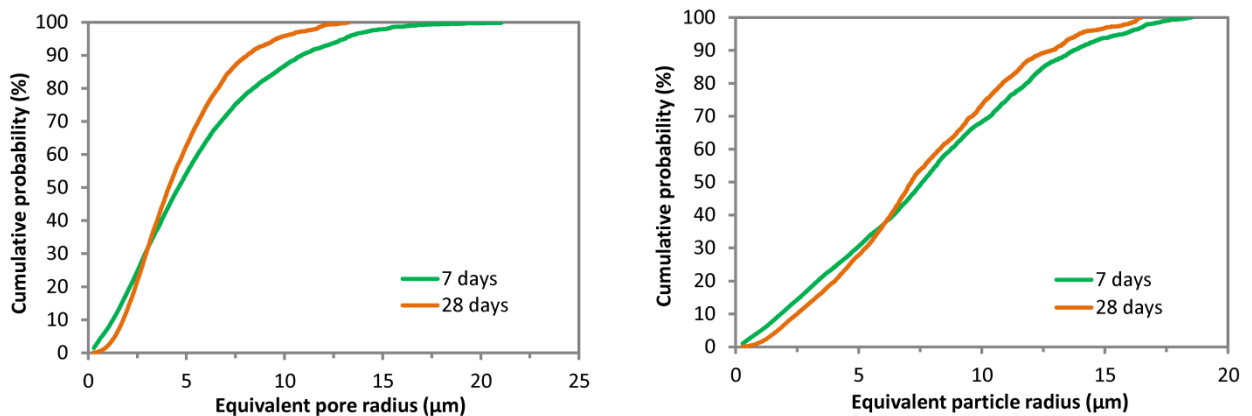
Figure 3: Microstructure properties of cement paste obtained by image analysis: pore size distribution (left); particle size distribution (right)

These data is used to construct models as described in Section 2. The calibration of the spring constants has been performed with the cement elastic properties at curing age of 28

days, i.e. at 12.58% porosity. From the calibration, the predicted Young's modulus as a function of porosity is given Fig. 4. The relation is approximately linear in the porosity range typical for cements and the result is consistent with the experimental finding in [17]. It should be noted, however, that at very small porosities the relation deviates from linearity, which is also consistent with previous reports on porosity effects on elastic constants [18].
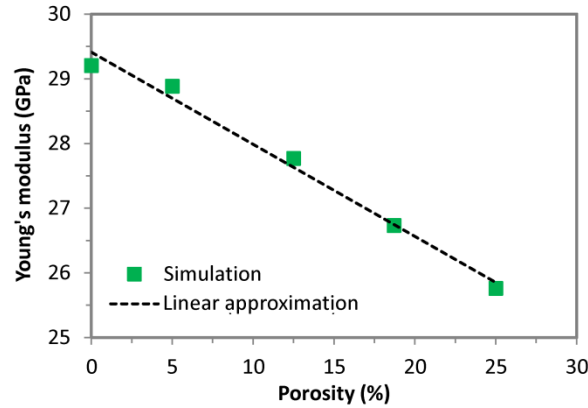
Figure 4: Predicted porosity dependence of Young's modulus of cement paste

For the simulations of mechanical behaviour of the cement paste with micro-cracking the energy of separation is 50 mJ / m^2. The simulated stress-strain curves under uniaxial tensile loading and the corresponding macroscopic damage evolution at different curing ages, i.e. 7 days and 28 days, is shown in Fig. 5. Compared to 7-day old cement paste, 28-day cement paste possesses a stronger nonlinearity prior to the final failure, and has a higher peak strain and tensile strength, which are mainly due to the different pore systems of two samples, as shown in Fig. 3. It can be seen that 7-day old cement paste contains much more "large" pores with sizes ranging from 10 to 20 μm. The bonds with such "large" pores tend to fail earlier due to the smaller effective surface area, which represents the initiation of micro-cracks in the sample. As the loading increases, these local micro-cracks propagate and coalesce much more easily. As a result, the macroscopic damage in 7-day old cement paste is less than that in 28-day old cement, i.e. less energy is dissipated prior to failure.
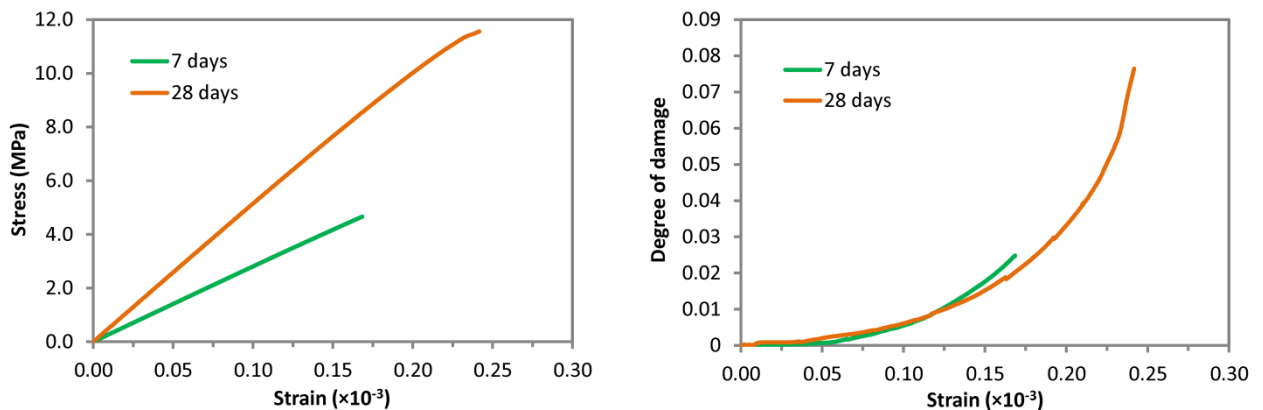
Figure 5: Stress-strain curves (left) and damage evolution (right) in cement pastes under uniaxial tension

The effect of porosity on the tensile strength of cement paste is studied by models with identical pore size distribution, particle size distribution and particle density but different porosities ranging from 8% to 35%. The obtained relationship between tensile strength and porosity is shown in Fig. 6 along with the available experimental data [19]. A good agreement between the simulations is demonstrated, especially for porosities higher than 20%.
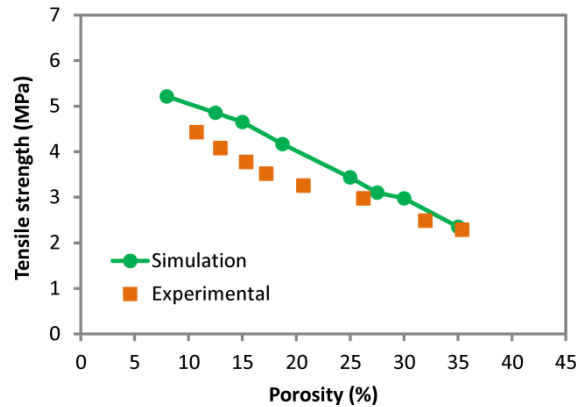
Figure 6: Simulated and experimental tensile strength-porosity relation in Portland cement paste

4.2 Nuclear graphite

The studies on nuclear graphite were based on two grades of graphite of differing microstructure, both developed for use in high temperature reactors; IG110 graphite (manufactured by Toyo Tanso, Japan) and PGX graphite (manufactured by Gratech, USA). The microstructure data used to populate the site-bond model was recreated from reported optical imaging results [20]. The distribution of pore sizes used for each graphite grade was recreated from the empirical expression given in [20] with the resulting cumulative probability distribution shown in Fig. 7. The upper limit of pore sizes was set at 1000μm, with only a tiny amount of larger pores discounted with this assumption. For briefness only the results for IG110 are shown here; detailed comparison of both grades is given in [12].
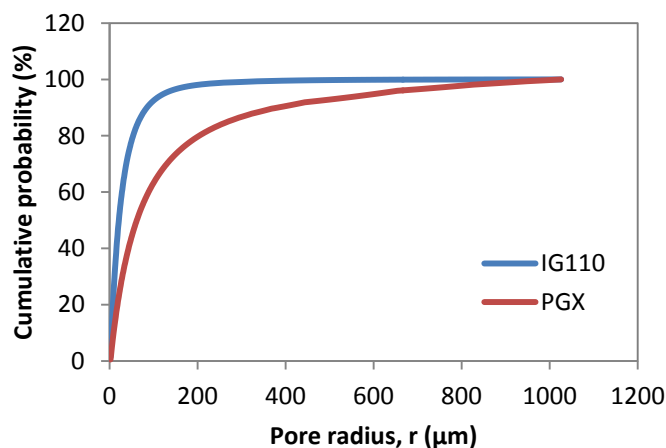
Figure 7: Cumulative probability function of pore sizes used for two graphite grade, recreated from [20].

The size of filler particles was assumed to follow a log-normal distribution with the required fitting parameters given in Table. 1. The porosity of IG110 graphite in the virgin state is 14.73% and this may grow to 60% when the graphite is irradiated in service. The particle volume fraction is 20% and does not change with irradiation. In reality, the increase of porosity with irradiation does not leave the pore size distribution shown in Fig. 7 unaffected. Evidence suggests that the proportion of smaller pores increases. However, there is not yet reliable data for the changes in the size distribution. Therefore, in this work the effect of irradiation is introduced solely by increasing the pore volume fraction from virgin state to highly irradiated state while keeping constant cumulative probability of pore sizes.

Table 1: Microstructure parameters and macroscopic elastic data for nuclear graphite IG110

Graphite grade	Mean particle diameter (μm) [20]	Standard deviation (μm) [20]	Young's modulus, E (MPa) [21]	Poisson's ratio, ν [21]
IG110	27	22	9800	0.14

The predicted stress-strain response and damage evolution in the graphite at different porosities are shown in Fig. 8. It can be seen that at lower porosities the failure is the typical 'graceful' failure characteristic of quasi-brittle materials. As the porosity is increased, representing different levels of radiation damage, the failure changes to a more glass-like brittle fracture with minimal damage and energy dissipation before failure. The failure in these cases is of "avalanche" type by simultaneous rupture of a set of critical bonds.
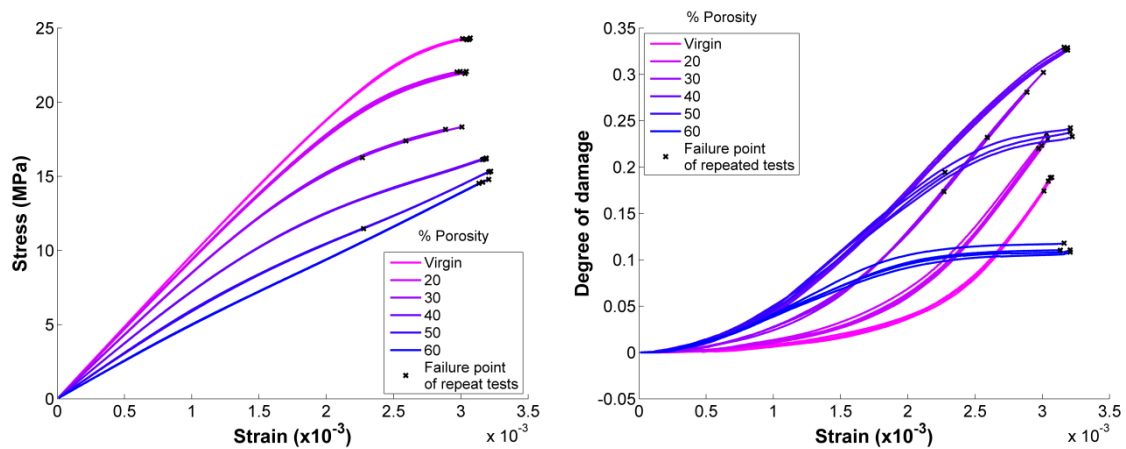
Figure 8: Stress-strain curves (left) and damage evolution (right) in IG110 graphite under uniaxial tension

The tensile strength has been shown experimentally to decay exponentially with increased porosity [22, 23]. According to the Knudsen phenomenological relation [24] the strength approaches zero at large porosities. The results obtained from our model, shown in Fig. 9, follow a similar exponential decay, but the end value is not zero. The reason for this is the resistance to instantaneous failure due to a number of bonds without pores even at high porosities. Even for avalanche failure, the system requires external work to overcome the failure energies assigned to these bonds. Larger porosities may improve this estimate.
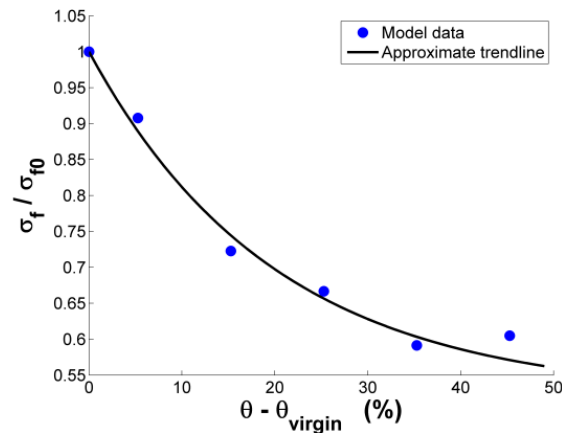
Figure 9: Simulated tensile strength-porosity relation for IG110 graphite

5   CONCLUSIONS

- Faithful mapping of microstructure features to a regular cell complex is presented for three-phase quasi-brittle media;
- Reduction of the cell complex to a site-bond model with spatially distributed bond mechanical properties is described;
- Graph-based formulation of the site-bond model is given together with the associated solution of boundary value problems by discrete exterior calculus;
- Results obtained with the proposed methodology are shown to be in good agreement with experiments for two different media – both in terms of elasticity-porosity relations and in terms of porosity effects on stress-strain behaviour and strength;
- The methodology can be used to derive macroscopic parameters from underlying microstructure features.

REFERENCES

[1] Carol, I., Jirasek, M. and Bazant, Z. A thermodynamically consistent approach to microplane theory. Part I. Free energy and consistent microplane stress. *Int. J. Solids Struct.* (2001) **38**: 2921-2931.

[2] Cusatis, G., Pelessone, D. and Mencarelli, A. Lattice discrete particle model (LDPM) for failure behaviour of concrete. I: Theory. *Cement Concr. Compos.* (2011) **33**: 881-890.

[3] Griffiths, D.V. and Mustoe, G.G.W. Modelling of elastic continua using a grillage of structural elements based on discrete element concepts. *Int. J. Num. Meth. Engng* (2001) **50**: 1759-1775.

[4] Karihaloo, B.L., Shao, P.F. and Xiao, Q.Z. Lattice modelling of the failure of particle composites. *Eng. Fract. Mech.* (2003) **70**: 2385-2406.

[5] Wang, Y. and Mora, P.. Macroscopic elastic properties of regular lattices. *J. Mech. Phys. Solids* (2008) **56**: 3459-3474.

[6] Schlangen, E. and van Mier, J.G.M. Experimental and numerical analysis of micromechanisms of fracture of cement-based composites. *Cement Concr. Compos.* (1992) **14**: 105-118.

[7] Liu, J.X., Zhao, Z.Y., Deng, S.C. and Liang, N.G. Numerical investigation of crack

growth in concrete subjected to compression by the generalised beam lattice model. *Comput. Mech.* (2009) **43**: 277-295.

[8] Jivkov, A.P. and Yates, J.R. Elastic behaviour of a regular lattice for meso-scale modelling of solids. *Int. J. Solids Struct.* (2012) **49**: 3089-3099.

[9] Jivkov A.P., Gunther, M. and Travis, K.P. Site-bond modelling of porous quasi-brittle media. *Mineral. Mag.* (2012) **76**: 2969-2974.

[10] Jivkov, A.P., Engelberg, D.L., Stein, R. and Petkovski, M. Pore space and brittle damage evolution in concrete. *Eng. Fract. Mech.* (2013) **110**: 378-395.

[11] Zhang, M., Morrison, C.N. and Jivkov, A.P. A meso-scale site-bond model for elasticity: Theory and calibration. *Mater. Res. Innov.* (2014) **in press**.

[12] Morrison, C.N. Zhang, M., Jivkov, A.P. and Yates, J.R. A discrete lattice model of quasi-brittle fracture in porous graphite. *Mater. Perform. Char.* (2014) **in press**.

[13] L.J. Grady and J.R. Polimeni, *Discrete calculus: Applied analysis on graphs for computational science*, Springer (2010).

[14] Shenoy, V.B. Atomistic calculations of elastic properties of metallic fcc crystal surfaces. *Phys. Rev. B* (2005) **71**: 094104.

[15] Javili, A. and Steinmann, P. On thermomechanical solids with boundary structures. *Int. J. Solids Struct.* (2010) **47**: 3245-3253.

[16] Zhang, M., He, Y., Ye, G., Lange, D.A. and van Breugel, K. Computational investigation on mass diffusivity in Portland cement paste based on X-ray computed microtomography (µCT) image. *Constr. Build. Mater.* (2012) **27**: 472-481.

[17] Haecker, C.J., Garboczi, E.J., Bullard, J.W., Bohn, R.B., Sun, Z., Shah, S.P. and Voigt, T. Modeling the linear elastic properties of Portland cement paste. *Cem. Concr. Res.* (2005) **35**: 1948-1960.

[18] Wang, J.C. Young's modulus of porous materials. *J. Mater. Sci.* (1984) **19**: 801-808.

[19] Chen, X., Wu, S. and Zhou, J. Influence of porosity on compressive and tensile strength of cement mortar. *Constr. Build. Mater.* (2013) **40**: 869-874.

[20] Kane, J., Karthik, C., Butt, D.P., Windes, W.E. and Ubic, R. Microstructural characterization and pore structure analysis of nuclear graphite. *J. Nucl. Mater.* (2011) **415**: 189-197

[21] Toyo Tanso Carbon Products. Special Graphite and Compound Material Properties.

[22] Ishihara, M., Sumita, J., Shibata, T., Iyoku, T. and Oku, T. Principle design and data of graphite components. *Nucl. Eng. Des.* (2004) **233**: 251–260.

[23] Berre, C., Fok, S.L., Mummery, P.M., Ali, J., Marsden, B.J., Marrow, T.J. and Neighbour, G.B. Failure analysis of the effects of porosity in thermally oxidised nuclear graphite using finite element modelling. *J. Nucl. Mater.* (2008) **381**: 1–8.

[24] Knudsen, F.P. Dependence of Mechanical Strength of Brittle Polycrystalline Specimens on Porosity and Grain Size. *J. Amer. Ceram. Soc.* (1959) **42**: 376–387.